ACKNOWLEDGMENTS

First and foremost, I would like to express my appreciation to my advisor, Dr. José Schutt-Ainé, for his attention, guidance, and insight during my thesis research.

Many thanks to my research group colleagues and friends, Johnson Liu, Edward Lee, Yidnek Mekonnen, and Pavle Milosevic, for their swift assistance with numerous technical aspects of this thesis.

I acknowledge the Department of Electrical and Computer Engineering of the University of Illinois at Urbana-Champaign for providing me with financial support during my graduate studies.

Finally, I am forever indebted to my parents and my wife Daria for their love and support.

TABLE OF CONTENTS

LIST OF FIGURES

CHAPTER 1

INTRODUCTION

1.1 Background

Electromagnetic modeling plays an important role in the design of electronic packages. As speed and/or frequency of high-performance circuits increases, much effort has been placed on the performance of interconnects and package structures driven by very short pulse signals. Increasing interconnection densities combined with high-speed circuit cells have exacerbated problems such as time delay, signal degradation, clock skew, and crosstalk, in the electronic packages. Thus, accurate modeling of these interconnection structures and circuit elements is necessary to ensure correct simulation of electrical performance at the design stage. When signal speed increases, high-frequency components of the signal must be taken into account. High-frequency effects, such as the appearance of longitudinal field components, are no longer negligible. The full-wave nature of the circuit components and interconnects becomes important. Therefore, a frequency-dependent circuit modeling based upon full-wave analysis is necessary [1].

A number of numerical techniques capable of highly accurate modeling of electromagnetic phenomena have been developed over the past years in tandem with the progress of computer technology. The list of the most popular ones includes the method of moments (MoM) [2] and finite element method (FEM) [3] in the

frequency domain and the transmission line matrix (TLM) [4] method and finite-difference time-domain (FDTD) method [5] in the time domain.

1.2 Motivation

The finite-difference time-domain (FDTD) method is arguably the simplest, both conceptually and in terms of implementation, of the full-wave techniques used to solve problems in electromagnetics. In essence, it is a direct solution method for Maxwell's differential (curl) equations in time domain. The method employs no potentials. Rather, it is based upon volumetric sampling of the unknown electric field vector **E** and magnetic field vector **H** within and surrounding the structure of interest, and over a period of time. The FDTD method uses finite difference approximations to both the spatial and temporal derivatives that appear in Maxwell's equations (specifically Ampere's and Faraday's laws). It is a marching-in-time procedure that simulates the continuous actual electromagnetic waves in a finite spatial region by sampled-data numerical analogs propagating in a computer data space. Time-stepping continues as the numerical wave analogs propagate in the space lattice to causally connect the physics of the modeled region. Time-stepping is carried on until the desired late-time pulse response is observed at the field points of interest [5].

There are several primary reasons for the expansion of interest in FDTD and related computational solution approaches for Maxwell's equations:

- FDTD uses no linear algebra. Being a fully explicit computation, FDTD avoids the difficulties with linear algebra that limit the size of frequency domain integral-equation and finite-element electromagnetic models.

- FDTD treats impulsive behavior naturally. Being a time-domain technique, FDTD directly calculates the impulse response of an electromagnetic system. Therefore, a single FDTD simulation can provide either ultrawideband temporal waveforms or the sinusoidal steady-state response at any frequency within the excitation spectrum.

- FDTD is a systematic approach. With FDTD, specifying a new structure to be modeled is reduced to a problem of mesh generation rather than the potentially complex reformulation of the equations describing the model.

- Computer memory capacities are increasing rapidly. Computers are getting faster and more powerful. While this trend positively influences all numerical techniques, it is of particular advantage to FDTD methods, which are founded on discretizing space over a volume, and therefore require a large random access memory.

- Computer visualization capabilities are increasing rapidly. It is again of particular advantage to FDTD methods, which generate time-marching arrays of field quantities suitable for use in color videos to illustrate the field dynamics.

With the increase in speed of modern integrated circuits, shrinking of their dimensions, and consequent increase in levels of integration, the modeling of interconnects and the simulation of transients have become of prime importance in the design process. In particular, characterization of the microstrip lines, which represent the most commonly used type of interconnect, is essential for the determination of an optimized layout scheme for printed circuit boards, chip carriers, or LSI (large-scale integration) chips found in most of today's high-speed digital networks.

To accurately model modern high-speed circuits, fully accounting for such phenomena as fringing, coupling, and radiation it is often necessary to simulate the

entire structure in one computation. The FDTD method can be used to perform such simulations. It is capable of effectively calculating frequency-dependent characteristics of microstrip interconnects, and it shows great promise in its flexibility in handling a variety of circuit configurations [6].

1.3 Contents

The material presented in this thesis is organized in two main parts. First an overview of the method is given, which includes formulation of the algorithm for one-, two-, and three-dimensional cases as well as discussion of such issues as stability of the method, truncation of problem space, and methods of source implementation in different cases. Along with the formulation of the key points, results of the corresponding FDTD simulations are presented.

In the second part application of the FDTD method to the simulation of various microstrip devices is explored; results of the simulations are compared to the measured data and also to the results of the simulation using a commercial electromagnetic simulator Agilent ADS Momentum.

CHAPTER 2

OVERVIEW OF THE METHOD

2.1 Finite Differencing Formulas

The basic idea of the finite difference method is in approximation of derivatives in partial differential equations. This approximation can be obtained directly from the well-known definition of the derivatives as the relation of a very small increase in a value of a function to a very small increase of a variable. This yields

$$f'(x) = \frac{df}{dx} \approx \frac{f(x + \Delta x) - f(x)}{\Delta x} \tag{2.1}$$

which is called the forward differencing formula. Similarly, we can decrease x and obtain the backward differencing formula

$$f'(x) = \frac{df}{dx} \approx \frac{f(x) - f(x - \Delta x)}{\Delta x} \tag{2.2}$$

We can also take the average of (2.1) and (2.2) to obtain

$$f'(x) = \frac{df}{dx} \approx \frac{f(x + \Delta x) - f(x - \Delta x)}{2\Delta x} \tag{2.3}$$

which is called the central differencing formula.

Using Taylor series it is easy to show [3] that approximations (2.1) and (2.2) are first-order accurate. Central differencing formula (2.3), on the other hand, is second-order accurate and is the most widely used differencing formula.

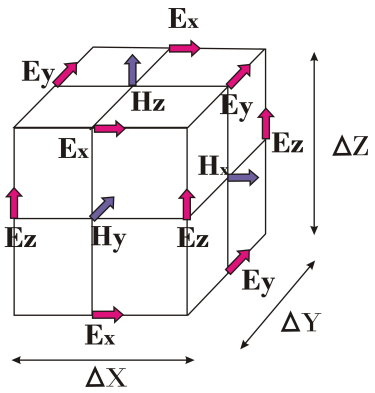

Figure 2.1: FDTD unit cell

2.2 The Yee Algorithm

Formulation of the FDTD method begins by considering the differential form of Maxwell's two curl equations which govern propagation of fields in the structures. For simplicity, the media are assumed to be lossless (i.e., no volume currents or finite conductivity). With these assumptions, Maxwell's curl equations may be written as

$$\mu \frac{\partial \mathbf{H}}{\partial t} = -\nabla \times \mathbf{E} \tag{2.4}$$

$$\epsilon \frac{\partial \mathbf{E}}{\partial t} = \nabla \times \mathbf{H} \tag{2.5}$$

To obtain discrete approximation to these continuous partial differential equations, central difference approximation is used. For convenience, the six field locations are considered to be interleaved in space as shown in Figure 2.1, which is a drawing of the FDTD unit cell.

The entire computational domain is obtained by stacking these cells into a larger rectangular volume. To emphasize this arrangement, E- and H-field components are assumed to be located at one half spatial step from each other. In a similar manner, field components are staggered in time, a half temporal step apart, in order to achieve centered differences for the time derivatives.

The FDTD algorithm was first proposed by Kane Yee [7]. The algorithm can be summarized as follows [8]:

1. Replace all the derivatives in Ampere's and Faraday's laws with finite differences. Discretize space and time so that the electric and magnetic fields are staggered in both space and time.

2. Solve the resulting difference equations for "future" fields in terms of "past" fields. That is to say, solve for fields at time $(n+1/2)\Delta t$ in terms of field at time $n\Delta t$ or $(n-1/2)\Delta t$.

3. Evaluate the future magnetic fields so they are known (effectively they become past fields).

4. Evaluate the future electric fields so they are known (effectively they become past fields).

5. Repeat the previous two steps until the desired duration has been achieved.

To clarify the above concept we will first consider a case of one-dimensional wave propagation. The extension to higher dimensions is straightforward.

2.3 One-Dimensional Formulation

Consider a one-dimensional space where there are only variations in the z direction [9]. In that case (2.4) and (2.5) produce only two scalar equations

$$\frac{\partial H_y}{\partial t} = -\frac{1}{\mu}\frac{\partial E_x}{\partial z} \tag{2.6}$$

$$\frac{\partial E_z}{\partial t} = -\frac{1}{\epsilon}\frac{\partial H_y}{\partial z} \tag{2.7}$$

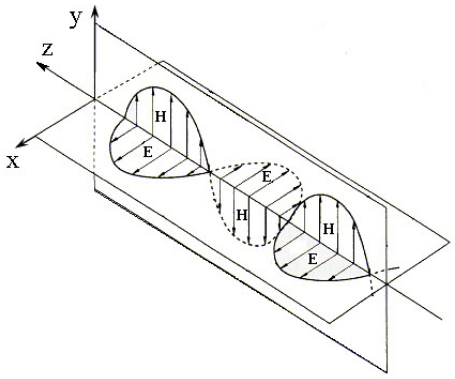

Figure 2.2: Plane wave

These are the equations of a plane wave with the electric field oriented in the x direction, the magnetic field oriented in the y direction, and traveling in the z direction as depicted in Figure 2.2.

Taking the central difference approximation for both the temporal and spatial derivatives in (2.6) and (2.7) gives

$$\frac{E_x|_k^{n+1/2} - E_x|_k^{n-1/2}}{\Delta t} = -\frac{1}{\epsilon}\frac{H_y|_{k+1/2}^n - H_y|_{k-1/2}^n}{\Delta x} \tag{2.8}$$

$$\frac{H_y|_{k+1/2}^{n+1} - H_y|_{k+1/2}^n}{\Delta t} = -\frac{1}{\mu}\frac{E_x|_{k+1}^{n+1/2} - E_x|_k^{n+1/2}}{\Delta x} \tag{2.9}$$

In (2.8) and (2.9), time is specified by the superscripts, while subscripts represent positions in discreet space. Figure 2.3 shows the sequence of field components computation interleaved in space and time.

Equations (2.8) and (2.9) can be rearranged in an iterative algorithm

$$E_x|_k^{n+1/2} = E_x|_k^{n-1/2} - \frac{1}{\epsilon}\frac{\Delta t}{\Delta x}\left[H_y|_{k+1/2}^n - H_y|_{k-1/2}^n\right] \tag{2.10}$$

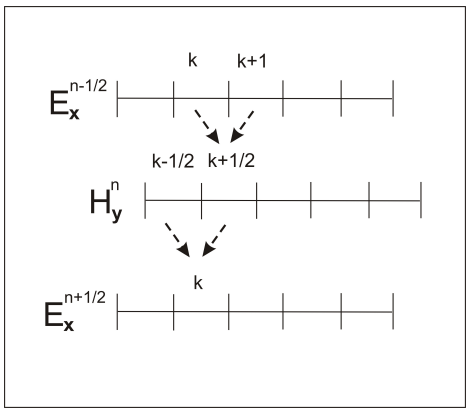

Figure 2.3: A diagram of the calculation of E and H fields in FDTD

```
ex[k] = ex[k] + ce*(hy[k-1] - hy[k]);
hy[k] = hy[k] + ch*(ex[k] - ex[k+1]);
```

Figure 2.4: One-dimensional update scheme

$$H_y|_{k+1/2}^{n+1} = H_y|_{k+1/2}^{n} - \frac{1}{\mu}\frac{\Delta t}{\Delta x}\left[E_x|_{k+1}^{n+1/2} - E_x|_{k}^{n+1/2}\right] \tag{2.11}$$

Again, the values of E and H are interleaved in both time and space. In (2.10) the new value of E_x is calculated from the previous value of E_x and the current value of H_y. This is the fundamental paradigm of the FDTD method [7].

Equations (2.10) and (2.11) with a few adjustments can be easily implemented in computer code. Since fields in a computer simulation are stored in the form of arrays with integer indices, $(k+1/2)$ and $(k-1/2)$ are rounded off to (k) and $(k-1)$; we will assume that E_x nodes are located to the left of H_y nodes with the same spatial indices. Time is implicit in the FDTD method. A basic one-dimensional field update scheme can be written in C computer code as shown in Figure 2.4.

In this case we assume that medium being simulated is homogenious, then $\frac{1}{\epsilon}\frac{\Delta t}{\Delta x}$ and $\frac{1}{\mu}\frac{\Delta t}{\Delta x}$ are constant parameters of the simulation. In practice the update scheme is sometimes modified for convenience of implementation [9]. The following change of variables is made in (2.10) and (2.11):

```
//Start of the main time-stepping loop
    for (n=1; n <= MaxSTEP; n++)
     {
             T = T + 1;

//Electric field update
      for (k=1; k <= KE; k++)
       { ex[k] = ex[k] + .5*(hy[k-1] - hy[k]); }

//Gaussian pulse source at the center of the grid
       pulse = exp( -.5*( pow( (delay-T)/width, 2) ) );
       ex[kc] = pulse;

//Magnetic field update
      for (k=0; k <= KE-1; k++)
       { hy[k] = hy[k] + .5*(ex[k] - ex[k+1]); }

     }
//End of the main time-stepping loop
```

Figure 2.5: One-dimensional FDTD code

$$\tilde{E} = \sqrt{\frac{\epsilon_0}{\mu_0}} E \tag{2.12}$$

Substituting this into (2.10) and (2.11) gives

$$\tilde{E}_x|_k^{n+1/2} = \tilde{E}_x|_k^{n-1/2} - \frac{1}{\epsilon} \frac{1}{\sqrt{\epsilon_0 \mu_0}} \frac{\Delta t}{\Delta x} \left[H_y|_{k+1/2}^n - H_y|_{k-1/2}^n \right] \tag{2.13}$$

$$H_y|_{k+1/2}^{n+1} = H_y|_{k+1/2}^n - \frac{1}{\mu} \frac{1}{\sqrt{\epsilon_0 \mu_0}} \frac{\Delta t}{\Delta x} \left[\tilde{E}_x|_{k+1}^{n+1/2} - \tilde{E}_x|_k^{n+1/2} \right] \tag{2.14}$$

Then $\frac{1}{\sqrt{\epsilon_0 \mu_0}} \frac{\Delta t}{\Delta x}$ is simply set equal to $\frac{1}{2}$ (the reason for this will be explained later). With these modifications a simple one-dimensional simulation of wave propagation in free space can be performed using the code shown in Figure 2.5

To demonstrate the functionality of the code in Figure 2.5, we consider a simulation of a wave propagating in free space where there are 200 electric- and magnetic-field nodes. A source with Gaussian profile is set up in the center of the grid. As a result, a Gaussian pulse is generated in the center and propagates away in both

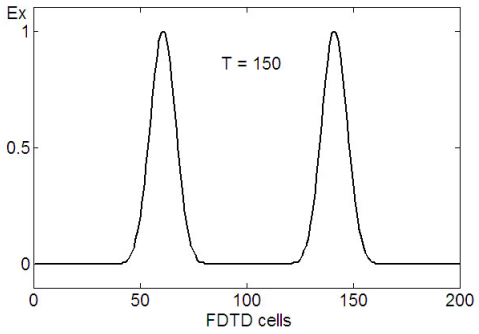

Figure 2.6: One-dimensional FDTD simulation

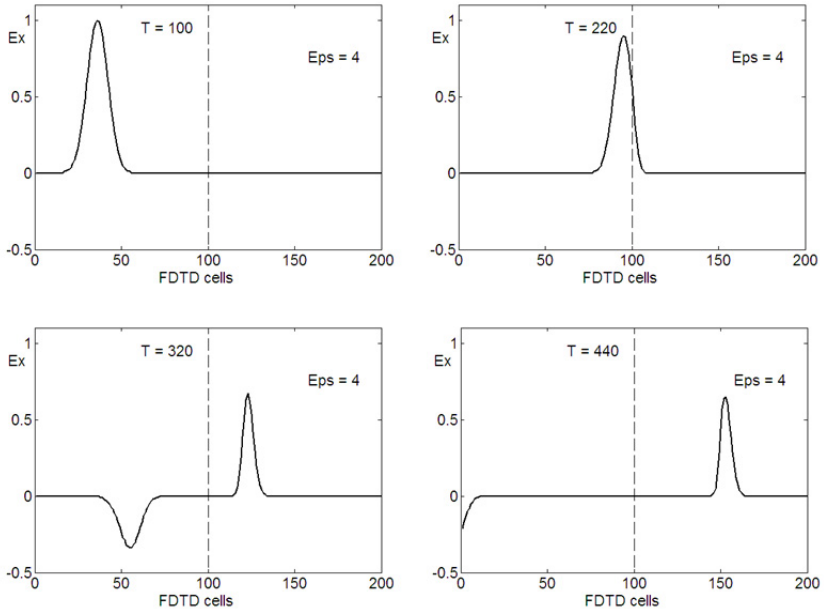

Figure 2.7: Simulation of a dielectric half space

directions. Figure 2.6 shows the snapshot of the normalized E_x field after 150 time steps.

In order to simulate a medium with a dielectric constant other than one, it is necessary to add the relative dielectric constant to update equations in 2.5. Figure 2.7 shows results of the simulation of a pulse traveling in free space until it strikes a dielectric medium. A portion of the pulse propagates into the medium and a portion is reflected.

```
//Ex field update

    for (i=0; i < XMAX; i++)
     {
       for (j=1; j < YMAX; j++)
        {
           for (k=1; k < ZMAX; k++)
            {
               curl_h = hz[i][j][k] - hz[i][j-1][k] - hy[i][j][k] + hy[i][j][k-1];
               ex[i][j][k] = ex[i][j][k] + 0.5*curl_h;
            }
        }
      }
```

Figure 2.8: Update of the E_x field component in three-dimensional FDTD simulation

2.4 Extension to Higher Dimensions

One of the advantages of the FDTD method is that extension to the higher dimensions is straightforward. The same discretization scheme and update equations are employed in two- and three-dimensional formulations. In full tree-dimensional case two Maxwell's vector curl equations (2.4), (2.5) can be written as

$$\mu \frac{\partial \mathbf{H}}{\partial t} = -\left(\hat{x}\left(\frac{\partial E_z}{\partial y} - \frac{\partial E_y}{\partial z}\right) + \hat{y}\left(\frac{\partial E_x}{\partial z} - \frac{\partial E_z}{\partial x}\right) + \hat{z}\left(\frac{\partial E_y}{\partial x} - \frac{\partial E_x}{\partial y}\right)\right) \tag{2.15}$$

$$\varepsilon \frac{\partial \mathbf{E}}{\partial t} = \left(\hat{x}\left(\frac{\partial H_z}{\partial y} - \frac{\partial H_y}{\partial z}\right) + \hat{y}\left(\frac{\partial H_x}{\partial z} - \frac{\partial H_z}{\partial x}\right) + \hat{z}\left(\frac{\partial H_y}{\partial x} - \frac{\partial H_x}{\partial y}\right)\right) \tag{2.16}$$

Equations (2.15) and (2.16) yield six scalar equations which can be fitted into the standard FDTD scheme. Figure 2.8 demonstrates a segment of code corresponding to calculation of E_x field in three-dimensional FDTD simulation.

Figure 2.9 illustrates three-dimensional pulse propagation. Again, a source is put in the center of the space, and Gaussian pulse propagates outwards. The figure shows distribution of the transverse component of electric field.

Results of the three-dimensional simulation look virtually the same as the two-dimensional ones, since only a "slice" of the space can be visualized.

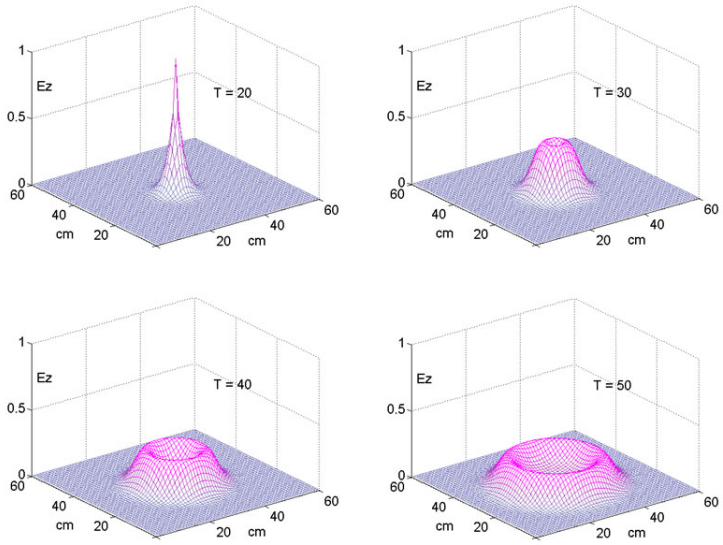

Figure 2.9: Three-dimensional simulation of a pulse in free space

2.5 Cell Size, Time Step, and Stability

The first step of the FDTD algorithm involves discretization of the computational space and time. Therefore, it is important to understand the restrictions associated with the choice of spacial and temporal steps. The size of a grid cell directly influences accuracy of the method. Theoretically, there is no lower limit for Δx; in fact, with $\Delta x \to 0$ FDTD solution becomes exact. However, infinitely fine discretization requires infinite computational resources. It can be shown that the number of floating point operations required for the simulation is proportional to $N^{3/4}$, where N is the total number of cells in the FDTD space. A common rule of thumb is to have at least 20 cells per wavelength at the highest frequency of interest. Another practical consideration is associated with geometry of the model. The mesh must adequately resolve the fine-scale geometric details of the structure, which is one of the main limiting factors of the FDTD method. Also, since the most natural and convenient shape of the lattice cell in the FDTD mesh is a cube, nonrectangular objects are modeled using staircase approximation, which can re-

quire the use of smaller lattice cells. The side length of a unit cubic cell is usually chosen to fit the critical dimensions of the model with an integer number of cells.

Once the spatial step is chosen, the choice of the temporal step is determined by the stability condition of the FDTD method. A classical approach to analyze numerical stability is the spectral technique developed by von Neumann. This method expresses the error in a numerical solution at any point in time as finite spatial Fourier series. Numerical stability results if each Fourier term has a unity-or-less growth factor over one time-step. However, even without carrying out a rigorous derivation, we can simply consider the way fields propagate in an FDTD grid. Since in the FDTD algorithm each node only affects its nearest neighbors, it is logical that energy in an FDTD grid should not be able to propagate any further than one spatial step for each temporal step, i.e., $c\Delta t \leq \Delta x$. The ratio $\frac{c\Delta t}{\Delta x}$ is referred to as the Courant number S_c [10]. For a one-dimensional simulation from the above discussion, it follows that the stability condition is $S_c \leq 1$. In a two-dimensional square-cell grid it takes two time steps to communicate information across the diagonal of the cell; and, as it takes three steps in the cubic three-dimensional lattice, consequently, the stability condition transforms into $S_c \leq 1/\sqrt{2}$ and $S_c \leq 1/\sqrt{3}$. The general expression for the stability condition is given by [11]

$$\Delta t \leq \frac{1}{c}\left(\frac{1}{\Delta x^2} + \frac{1}{\Delta y^2} + \frac{1}{\Delta z^2}\right)^{-1/2} \tag{2.17}$$

Since a larger time step means a shorter run time, it is desirable to use the maximum value of Δt. Also, it can be shown that the grid dispersion error is proportional to $\left(\sqrt{(\Delta x)^2 + (\Delta y)^2 + (\Delta z)^2}/\lambda\right)^2$ [12], hence maximizing Δt minimizes the dispersion. However, the condition in (2.17) is extremely rigorous, so that even slightest violation of the bound leads to instability and the computed results spuriously increase without limit during time-marching. For that reason,

due to a rounding error in the computer, in practice Δt is often set to a value just below the limit given by (2.17). A less optimal but convenient approach is to set $S_c = 0.5$, the way we did it in Section 2.3. Although not optimal, this choice is equally suitable for one-, two-, and three-dimensional simulations resulting in simple values of coefficients in update equations.

2.6 Source Setup in an FDTD Simulation

FDTD algorithms require initial conditions, which means that values of the fields must be specified throughout the lattice at the start of the simulation. Typically, all fields are initialized to zero. To perform a simulation, energy has to be introduced into the problem space; i.e., an electromagnetic wave source has to be created. The general classes of EM wave sources are:

1. Hard-sourced and fields in one- and two-dimensional grids;
2. Plane-wave excitation via total-field/scattered-field formulation in one, two, and three dimensions;
3. Lumped electronic circuit models of resistive voltage source.

A hard source is set up simply by assigning a desired time function to specific components of E and H fields in the FDTD space lattice. This time function is independent of anything else in the model. One of the most common pointwise hard sources provides a lowpass Gaussian pulse with finite dc content. Such a source was used to generate the snapshot depicted in Figure 2.9. The time waveform of the pulse is centered at time-step n_0 and has a $1/e$ characteristic decay of n_{decay} time-steps:

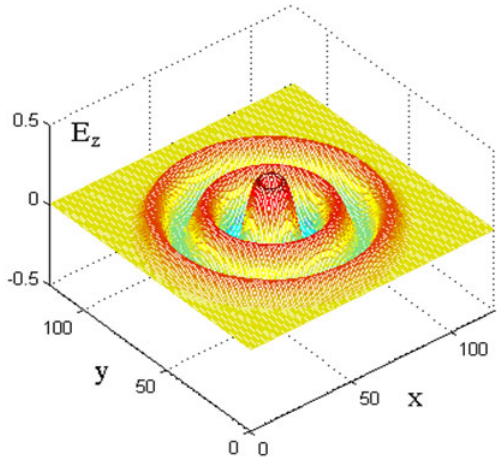

Figure 2.10: FDTD simulation of a sinusoidal source in free space

$$E_z|_{is}^n = E_0 e^{-\left[(n-n_0)/n_{decay}\right]^2} \tag{2.18}$$

E_z in (2.18) has a nonzero value at $n = 0$, so that if a smooth transition from zero into Gaussian pulse is required, n_0 should be taken as at least $3n_{decay}$. The value of n_{decay} controls the width of the pulse in time domain and correspondingly its bandwidth in frequency domain.

Another common hard source is a sinusoidal source, which generates a continuous sinusoidal wave of frequency f_0 that is switched on at $n = 0$:

$$E_z|_{is}^n = E_0 \sin\left(2\pi f_0 n \Delta t\right) \tag{2.19}$$

Each hard source radiates a numerical wave having a time waveform corresponding to the source function. A pointwise hard source located within a two-dimensional FDTD grid excites a radially propagating cylindrical wave centered on the source point. Figure 2.10 demonstrates radiation from a sinusoidal hard source governed by (2.19) in two-dimensional free space.

However, all hard sources have a major drawback. In prolonged simulations, waves reflected from the objects in the computational space eventually reach source points, whereupon spurious, nonphysical reflections occur. For example, the Gaussian point source specified by (2.18) decays to zero with time and then acts as a perfect electric conductor (PEC), causing spurious reflections. For this reason, using hard source in an FDTD simulation requires either limiting duration of the simulation or employing some scheme of removing the source from the computational domain.

An alternative way to realize a plane wave source that avoids the difficulties caused by using hard sources is the total-field / scattered-field (TF/SF) formulation [13]. The TF/SF formulation is based on linearity of Maxwell's equations. It assumes that the physical total electric and magnetic fields can be decomposed as follows:

$$\mathbf{E}_{total} = \mathbf{E}_{incident} + \mathbf{E}_{scattered} \qquad \mathbf{H}_{total} = \mathbf{H}_{incident} + \mathbf{H}_{scattered} \tag{2.20}$$

The FDTD lattice is subdivided into two regions as in Figure 2.11, Region 1 containing objects and total fields, and Region 2, in which only scattered fields are present.

The difference between fields in the two regions is the incident field. To maintain continuity of the tangential fields, incident field has to be subtracted or added at the boundary. This way, Regions 1 and 2 are separated by a nonphysical surface that serves to connect the fields in two regions, and thereby generates an incident wave. Incident field values can be generated by an auxiliary one-dimensional simulation and applied at the boundary surface, generating a plane wave with constant amplitude along the surface. Auxiliary simulation can be excited by a pointwise source with a user specified time function. Figure 2.12 illustrates generation of the

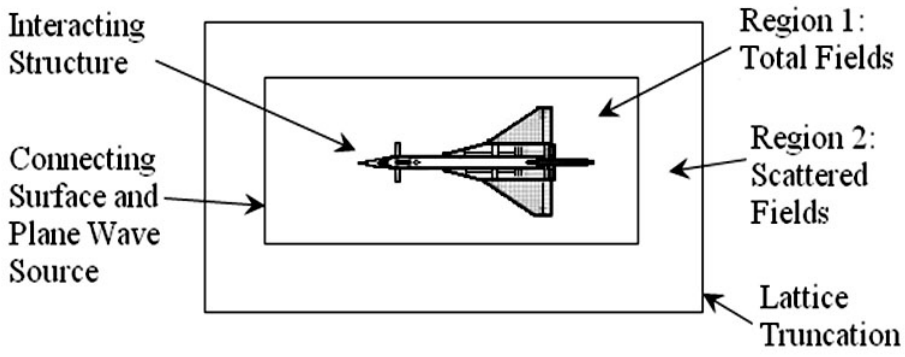

Figure 2.11: Total-field / scattered field zoning of the FDTD space lattice

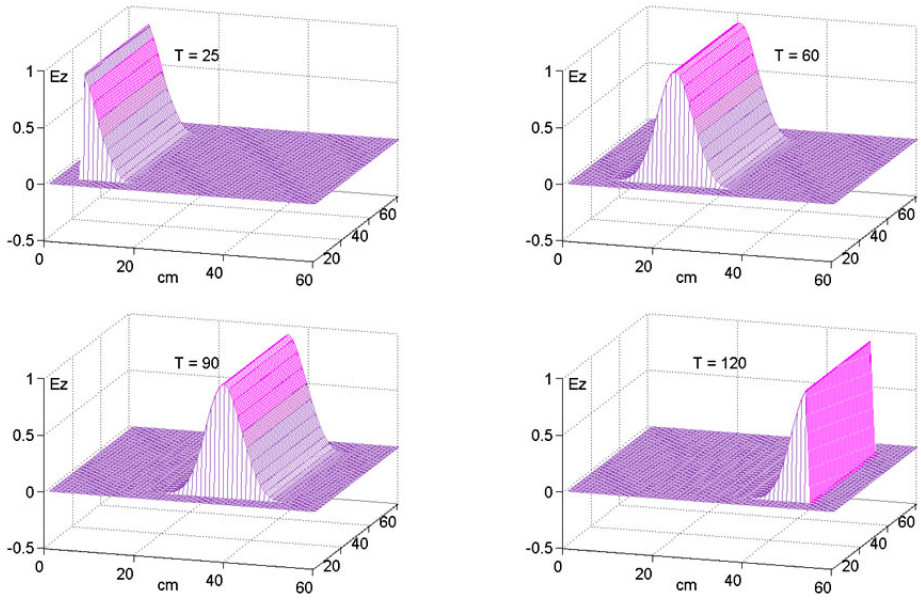

Figure 2.12: Simulation of a plane wave source using TF / SF formulation

plane wave with Gaussian profile using TF / SF boundary. The incident field is added at one end of the computational space and subtracted at the other end.

The major advantage of the TF / SF formulation is that the interface between the regions, which serves as a source of the incident wave, is transparent for the backward propagating waves scattered by objects in the total field region.

For the resistive source implementation the FDTD formulation is extended to allow for the addition of lumped linear and nonlinear circuit elements. Circuit

elements can be accounted for by adding a lumped electric current density term $\mathbf{J}_L$ to the conduction and displacement currents in Maxwell's curl equation for H-field resulting in

$$\nabla \times \mathbf{H} = \mathbf{J}_C + \frac{\partial \mathbf{D}}{\partial t} + \mathbf{J}_L \tag{2.21}$$

The resistive voltage source permits simulation of a source matched to a microstrip line.

2.7 Truncation of the FDTD Lattice

Many of electromagnetics problems require modeling of large or even infinite, unbounded problem space. Since it is obviously impossible to actually incorporate infinity into a computer simulation, FDTD lattice must be limited in size. Truncation of the FDTD computational space creates one immediate problem: each field node in the FDTD computation requires values of fields at neighboring nodes in the update scheme. However, nodes adjacent to the boundary of the lattice do not have neighbors since there is no information concerning fields outside of the computational space. This problem is solved by setting fields at the outermost nodes to a constant value and never updating them in the computation. In most cases a PEC bounding box is created. Construction of a PEC boundary creates another, less immediate, problem. Outgoing waves eventually reach the boundary and they are totally reflected back into the computational domain. Such spurious reflections contaminate the solution. The straightforward way to avoid this problem is to place domain boundaries very far from the region of interest. This solution is obviously very ineffective, especially for prolonged simulations. Hence, a suitable boundary condition is required, which permits all outward-propagating

numerical waves to exit the problem space as if the simulation were performed on a computational domain of infinite extent.

Depending upon their theoretical basis, outer-boundary conditions of this type are called either radiation boundary conditions (RBCs) or absorbing boundary conditions (ABCs). The notation ABC is usually used as a general term. ABCs can be roughly divided into two general types: (1) analytical ABCs, and (2) perfectly matched absorbing layers (PML). One of the most common analytical ABCs is Mur's ABC [14]. It is based on the finite-difference approximation of the one-way wave equation. When applied at the outer boundary of an FDTD computational space, a one-way wave equation numerically absorbs impinging outgoing waves. Another technique was developed by Higdon [15]. Higdon's approach involves the construction of a series of linear differential operators to annihilate outgoing numerical waves.

A popular alternative approach to realize ABCs is based on the idea that instead of constructing analytical absorbers it is possible to actually surround the computational domain with an absorbing material medium. This is analogous to the physical treatment of the walls of an anechoic chamber. Ideally, the absorbing medium is only a few lattice cells thick, reflectionless to all impinging waves over their full frequency spectrum, highly absorbing, and effective in the near field of a source or a scatterer.

To illustrate the idea behind PML absorber it is prudent to consider an interface between a homogeneous, dispersionless half-space (Region 1) and a conventional lossy medium (Region 2) having electric and magnetic conductivities $\sigma$and σ^*. A plane wave incident upon such an interface at angle θ_i is partially reflected and partially transmitted into the lossy medium. A ratio of reflected and incident fields or the reflection coefficient can be expressed as

$$\Gamma = \frac{\eta_1 \cos\theta_i - \eta_2 \cos\theta_t}{\eta_1 \cos\theta_i + \eta_2 \cos\theta_t} \tag{2.22}$$

In (2.22) η_1 and η_2 are the wave impedances in Regions 1 and 2, given by

$$\eta_1 = \sqrt{\frac{\mu_1}{\varepsilon_1}} \tag{2.23}$$

$$\eta_2 = \sqrt{\frac{\mu_2(1+\sigma^*/j\omega\mu_2)}{\varepsilon_2(1+\sigma/j\omega\varepsilon_2)}} \tag{2.24}$$

From (2.22) we can see that in general $\Gamma \neq 0$ for arbitrary angle θ_i. However, for the special case of normal incidence ($\theta_i = \theta_{ref} = \theta_{trans} = 0$), we have

$$\Gamma = \frac{\eta_1 - \eta_2}{\eta_1 + \eta_2} \tag{2.25}$$

Now, if we set $\epsilon_1 = \epsilon_2$, $\mu_1 = \mu_2$, and choose conductivities so that

$$\frac{\sigma^*}{\mu_1} = \frac{\sigma}{\varepsilon_1} \tag{2.26}$$

then $\eta_1 = \eta_2$. From (2.25) we can see that in this case for the normally impinging wave $\Gamma = 0$, and the Region 1 / Region 2 interface is reflectionless. Moreover, the wave in the lossy medium is quickly attenuated so that the medium can be used as the absorbing boundary.

However, a conventional lossy medium can be matched to the interior of the FDTD lattice only for the case of normal incidence. To be feasible the absorbing boundary must be matched for an arbitrary angle of incidence. The first formulation of such a reflectionless absorbing material was introduced by Berenger in 1994 [16]. Berenger called his absorber the perfectly matched layer (PML), emphasizing its reflectionless property. To achieve reflectionless condition for all angles of incidence, Berenger utilized artificial splitting of the fields into orthogonal sub-

components (the split-field formulation). A different implementation of the PML was later proposed by Sacks et al. [17]. The alternative formulation avoided non-physical field splitting. Instead, an anisotropic absorbing material was postulated, which was made perfectly reflectionless by the specific choice of permittivity and permeability tensors. Sacks et al. used their anisotropic PML with the FEM in frequency domain. Following the work by Sacks et al., Gedney formulated anisotropic PML for use with the FDTD method in time domain, which he called the Uniaxial PML (UPML) [18], [19]. A similar approach was used by Sullivan in formulation of the simplified PML [20].

Figure 2.13 demonstrates effectiveness of the PML. Snapshots of the E-field show how the sinusoidal source stays stable over time, with outgoing waves being absorbed by the PML. In case of the lattice terminated with PEC, spurious reflections destroy the field pattern.

To implement either simplified PML or UPML, a standard FDTD scheme is slightly altered. Within the PML layer, fields are updated in two steps: first D (electric flux density) is computed, then E (electric field intensity); and in the same way for magnetic field: first B (magnetic flux density), then H (magnetic field intensity) are calculated. PML material properties are represented by a set of coefficients in these update equations. A detailed description of computer implementation of the UPML can be found in [5]; the simplified PML is described in [9].

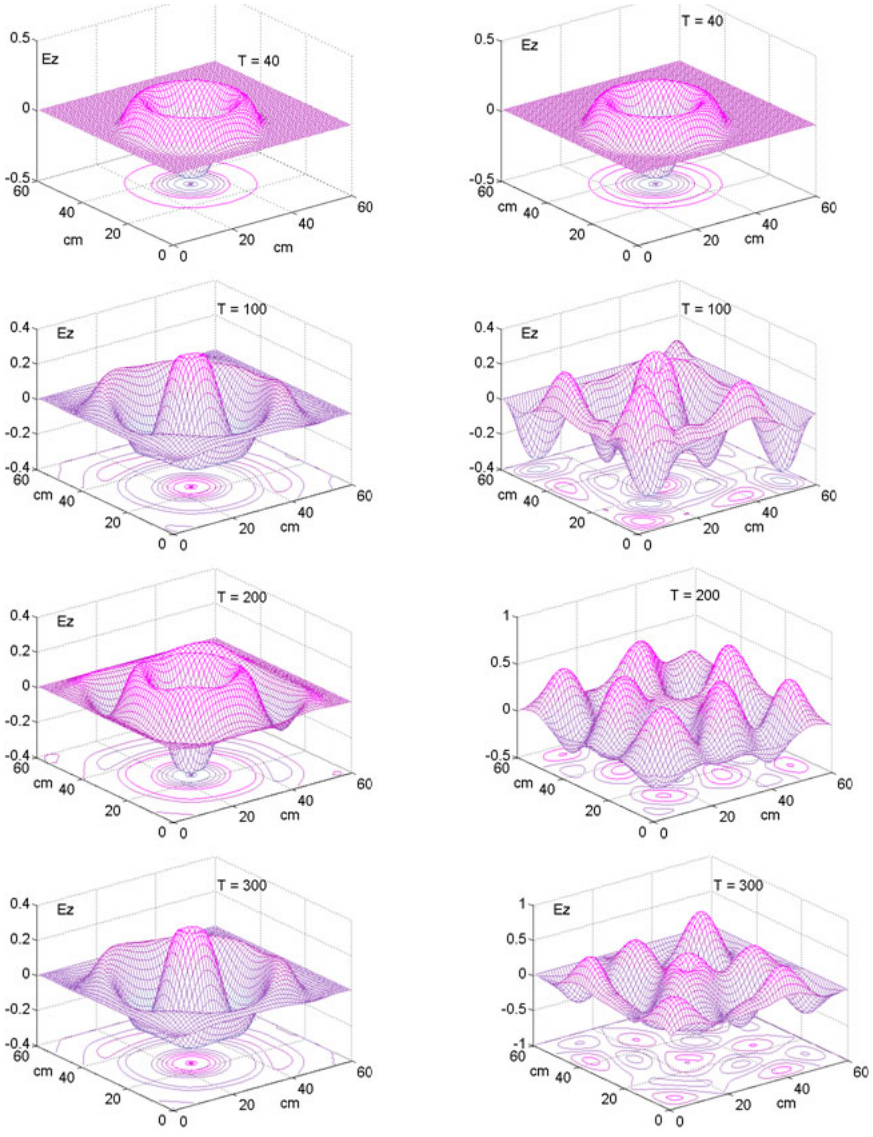

Figure 2.13: Sinusoidal source with (on the left) and without PML

CHAPTER 3

NUMERICAL RESULTS, MEASUREMENTS, AND OBSERVATIONS

3.1 Overview

A full-wave three-dimensional FDTD simulation engine was developed and used for simulation of a number of microstrip devices. The program was written in C computer code. Some MATLAB functions were also employed for data processing and visualization. The code functionality was first tested by the simulation of a microstrip antenna. Results of that simulation were compared with those presented by Sheen et al. in [6]. Then, a number of microstrip test boards were designed, simulated, manufactured, and measured. Results of the simulations were compared to the measured data. Additionally, some of the devices were simulated using a commercial electromagnetic simulator Agilent ADS Momentum.

3.2 Simulation of the Microstrip Antenna

To test the program, a simulation of a line-fed rectangular microstrip antenna was performed and scattering matrix coefficients for the antenna were computed. This problem is a popular benchmark used by many researchers. The original simulation was done by Sheen et al. [6], who also manufactured the device and measured it using HP 8510 network analyzer.

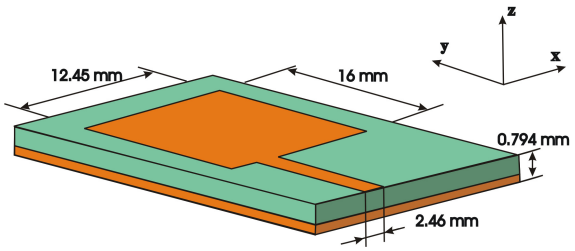

Figure 3.1: Line-fed microstrip antenna

3.2.1 Simulation setup

The simulation was set up closely following the work by Sheen et al. The microstrip antenna analyzed is shown in Figure 3.1.

Metal parts of the circuit were assumed to be perfectly lossless, i.e., perfect electric conductor (PEC) approximation was used. In the simulation tangential components of the electric field were set to zero at locations corresponding to metal parts of the circuit. Thickness of the metal was assumed to be negligible in comparison with thickness of the substrate. The circuit was constructed on the Duroid substrate with relative permittivity $\epsilon_r = 2.2$. Spatial step $\Delta z = 0.265\,\text{mm}$ was chosen to model the substrate thickness with exactly 3 cells. The time step used was $\Delta t = 0.441\,\text{ps}$.

A voltage source excitation was simulated using a hard source scheme. Vertical E_z field was imposed in a rectangular region underneath the feeding strip, between the strip and the ground plane. The Gaussian pulse was used for excitation. The source plane was put directly at the boundary of the computational domain.

The second order Higdon ABC was used for truncation of the lattice.

3.2.2 Results of the antenna simulation

Figure 3.2 shows the spatial distribution of $E_z(x, y, t)$ just beneath the microstrip at 100, 230, 330, and 410 time steps. Three-dimensional properties of the

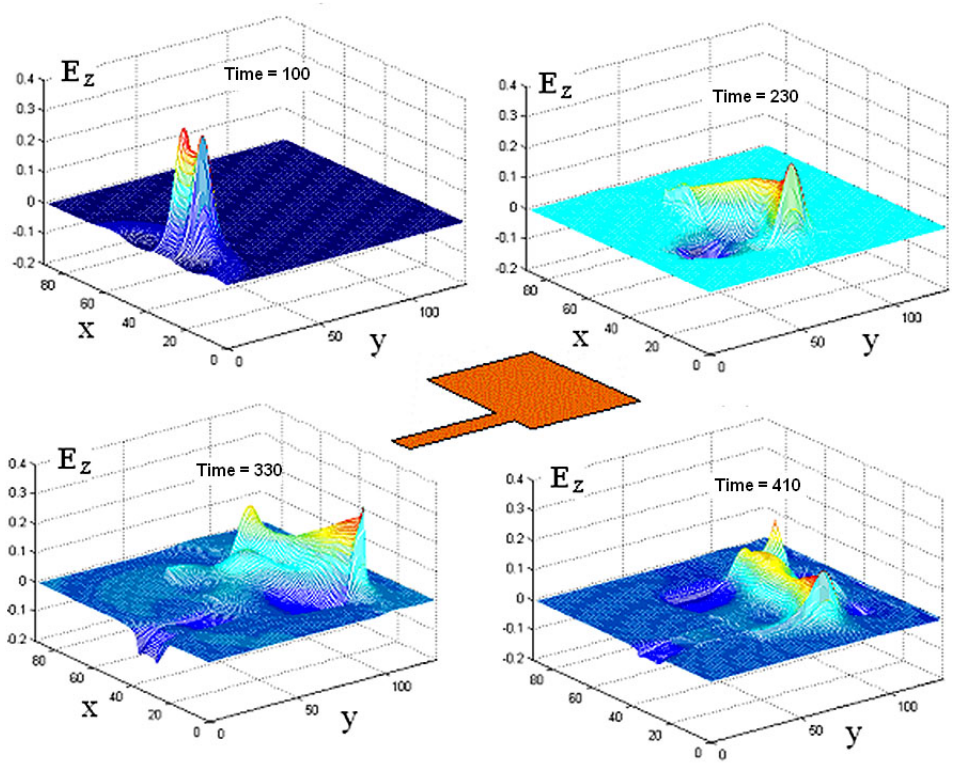

Figure 3.2: Snapshots of $E_z(x, y, t)$ at 100, 230, 330, and 410 steps

propagation are observed, including enhancement of the field near the edges of the microstrip.

The frequency-dependent scattering matrix coefficients can be easily calculated from the results of the simulation. The scattering matrix, or [S] matrix [21], is defined in relation to incident and reflected voltage waves as

$$[V]^{ref} = [S][V]^{inc} \tag{3.1}$$

The vertical electric field under the strip was recorded at each time-step. Under the assumption that voltage is proportional to the field value, the time-domain data recorded in the simulation can be treated as the sum of the incident and reflected voltage waves. To recover the incident field the simulation was performed for a microstrip line, which was extended to the far boundary of the computational do-

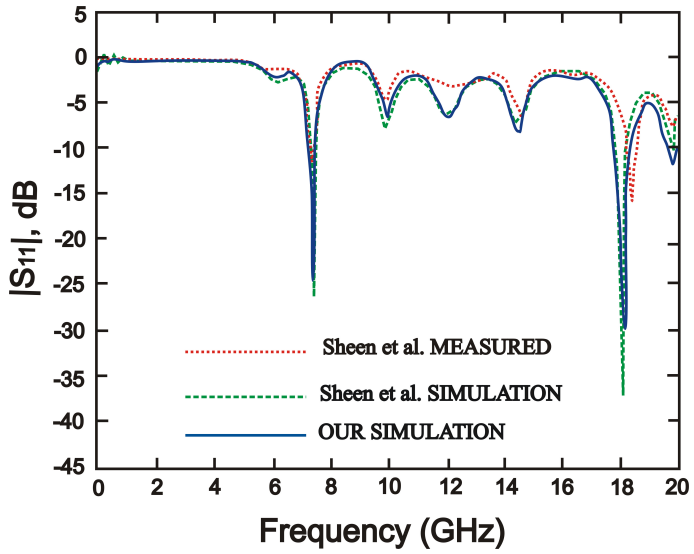

Figure 3.3: Magnitude of S_{11} parameters of the antenna

main. Then the reflected waveform was calculated by subtracting the results of the two simulations. Time-domain data was then processed using Fourier transform, and S_{11} parameters were calculated as the ratio of the reflected and incident waves at port 1

$$S_{11}(\omega) = \frac{F\{V_{1ref}(t)\}}{F\{V_{1inc}(t)\}} \tag{3.2}$$

The scattering coefficient results, shown in Figure 3.3, are in good agreement with the data obtained by Sheen et al. The operating resonance at 7.5 GHz is almost exactly shown by both theory and measurement; it corresponds to the frequency where the x-dimension of the antenna, 12.45 mm, is a half wavelength.

3.3 Modeling of Microstrip Traces

The FDTD code was modified and used to simulate a number of meandered microstrip traces. Meandered lines were chosen as test structures representing effects of bending, coupling, and radiation in circuit boards traces. To verify the results

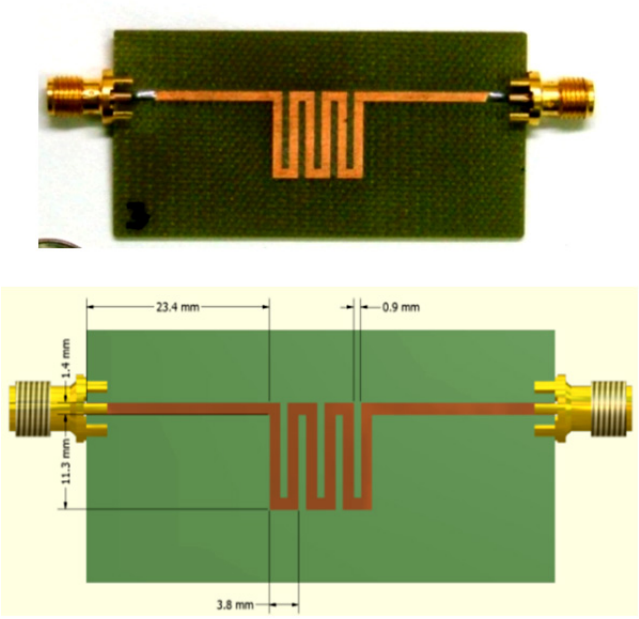

Figure 3.4: The test board

of numerical simulations, several test boards were manufactured and measured using Agilent E8363B PNA Network Analyzer. In this paper, results for one of the meandered lines are presented together with the results for a straight line with the same dimensions, which was used as a reference.

3.3.1 Simulation setup

Figure 3.4 shows the top view of the meandered line test structure.

All lines were constructed on FR4 substrate 61 mils thick. Board length was 60 mm, conductor width was 1.4 mm. Each board had two SMA connectors attached at the ends of the traces.

The FDTD code was modified to improve the accuracy of the simulation. Signals propagating through the meandered line experience numerous reflections; there is a strong coupling between closely spaced traces that form the meandered structure; also, a significant amount of energy is being radiated from the surface of the

meandered line. As a result, the load on the absorbing boundaries is increased. To avoid spurious reflections, a highly effective boundary condition, the perfectly matched absorbing layer was used for truncation of the computational domain. A form of uniaxial PML (UPML) proposed by Gedney [18] in modification derived by Sullivan [20] was implemented.

Voltage source used for the microstrip antenna simulation is difficult to use especially in conjunction with the PML ABC. Instead, a plane wave source based on the TF/SF formulation was implemented. A source plane was located between the conductor strip and the ground plane. TEM (transverse electromagnetic) incident wave was simulated.

In the simulation of the microstrip antenna it was assumed that the feeding microstrip had characteristic impedance of 50 Ohms, so that it was matched to the measuring system. Our test lines were designed to have characteristic impedance of 75 Ohms. Due to processing variations the actual impedance measured with time-domain reflectometer was approximately 73 Ohms. To account for the impedance discontinuity between measurement systems, connectors, and the test structures, short segments of 50-Ohm line were included in the model. The segments were placed at the ends of the test lines and extended into the absorbing boundary layer to simulate the 50-Ohm reference. Figure 3.5 shows the setup used for the simulation of the straight microstrip with a 50-Ohm reference.

In Figure 3.5, the structure between reference planes represents the device under test, the line. All dimensions are given in grid cells. In the x-direction 1 cell = 0.25 mm; in the y-direction 1 cell = 0.5 mm. The length of the actual board is 60 mm; external parts of the connectors soldered to the strip extend outside the board for about 1 mm each. So the distance of 124 cells (= 62 mm) between reference planes is justified.

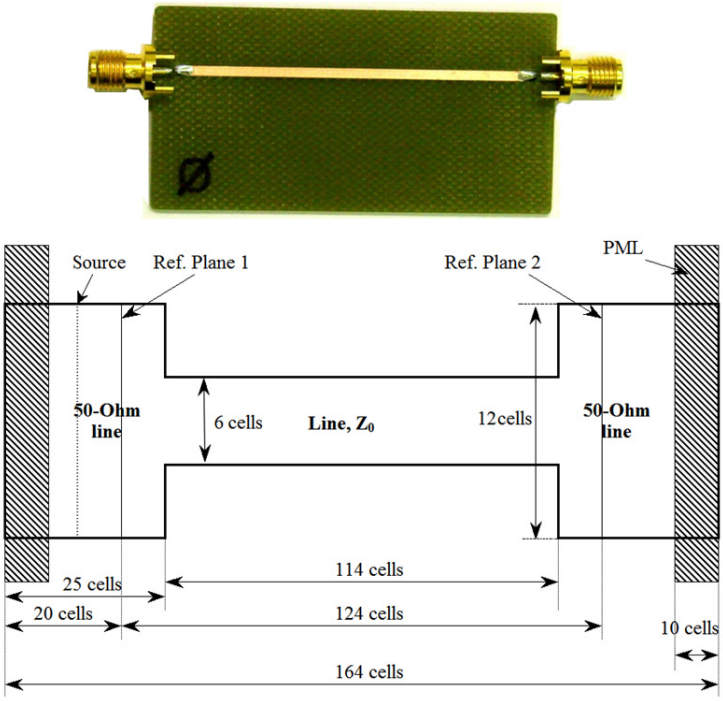

Figure 3.5: Simulation setup for the straight microstrip line

Reference planes must be placed at the 50-Ohm segments of the structure. It would seem natural to put them exactly at the edges of the 50-Ohm segments. However, placing a reference right at the discontinuity is not desirable. To avoid this, 50-Ohm segments are extended five cells inwards. We treat these extensions as representation of parts of connectors attached to the microstrip. The length of the connector's extensions is 2.5 mm.

3.3.2 Results and analysis

Magnitudes and phases of S_{11} and S_{21} parameters were computed for the meandered lines and the straight microstrip. The devices were assumed to be symmetrical and reciprocal, so that $S_{11} = S_{22}$ and $S_{21} = S_{12}$. The meandered lines were also simulated using Agilent ADS Momentum simulator.

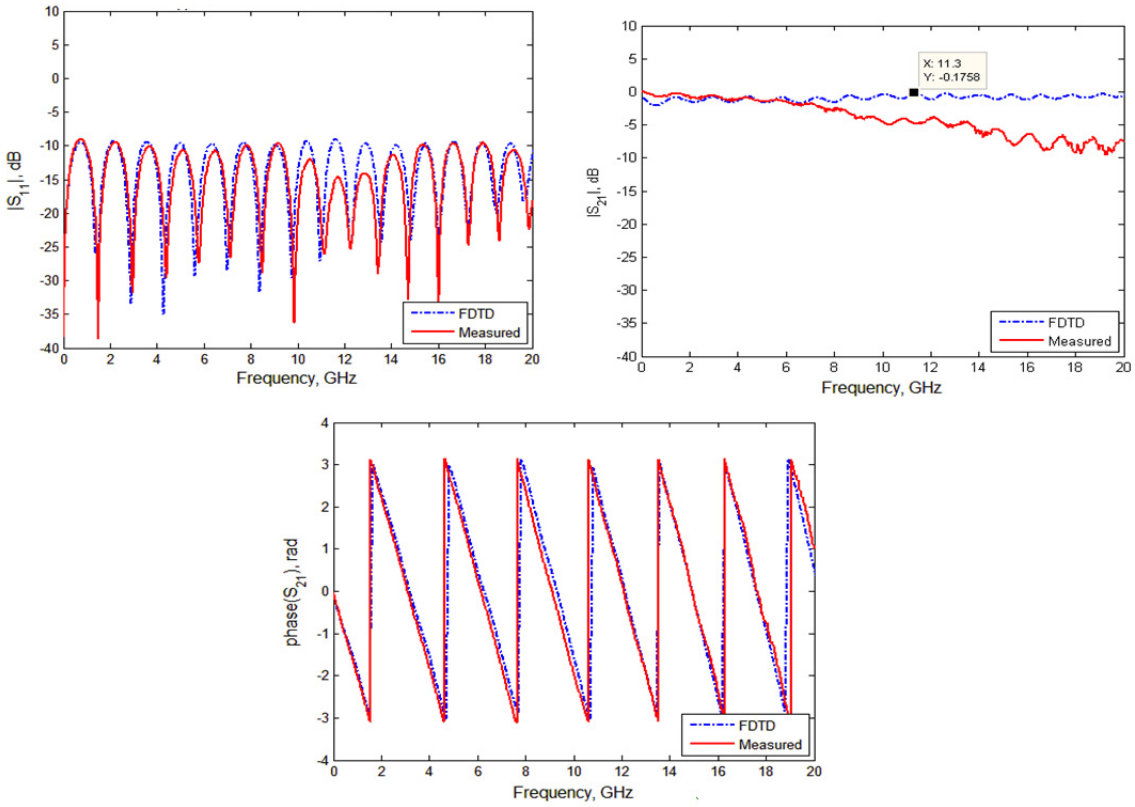

Figure 3.6: S-parameters of the straight line

Figure 3.6 shows the results of the straight line simulation together with the measured data.

From Figure 3.6 we can see that the magnitude of S_{11} of the straight line agrees very well with the measurement. Magnitude of S_{21} agrees with the measurement at frequencies below 7 GHz. At higher frequencies the skin effect causes the measured curve to deviate from the simulated one. Due to skin effect, resistance of the line increases with frequency lowering S_{21} (essentially the transmission coefficient). The curve obtained from the simulation stays at the same level over the whole range of frequencies, since in the simulation conductors are assumed to be perfectly lossless. Phase of S_{21} is in good agreement with the measurement, which means that the length of the line is modeled correctly.

Figure 3.7 shows the results for one of the meandered lines.

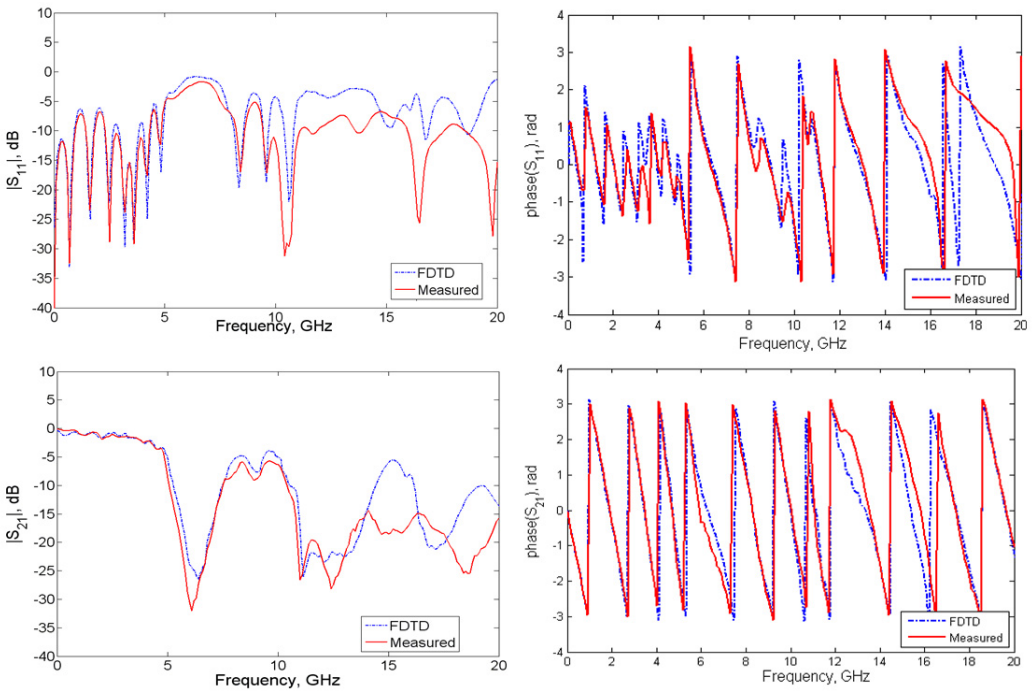

Figure 3.7: Magnitudes and phases of S-parameters of the meandered line

Results of the FDTD simulation are compared to the measurement. In general there is a good correlation between the FDTD simulation and the measurement is observed up to 12 GHz. At higher frequencies the agreement becomes rather poor. As was mentioned earlier, the FDTD model does not account for conductor loss, which is significant in the relatively long folded line, especially at high frequencies. Unaccounted substrate loss also contributes to the error. Finally, the dielectric constant of FR4 substrate, assumed to be constant in the model, in reality has strong frequency dependence. In general FR4 substrate is not used for very high frequency applications.

Results of the FDTD simulation were also compared to the simulated results obtained using the Agilent ADS Momentum simulator. Comparison of the FDTD simulation results with the results obtained from ADS Momentum shows very good correlation. At the same time, both simulators fail to predict the behavior of the test structure at frequencies above 12 GHz as it is shown in Figure 3.8.

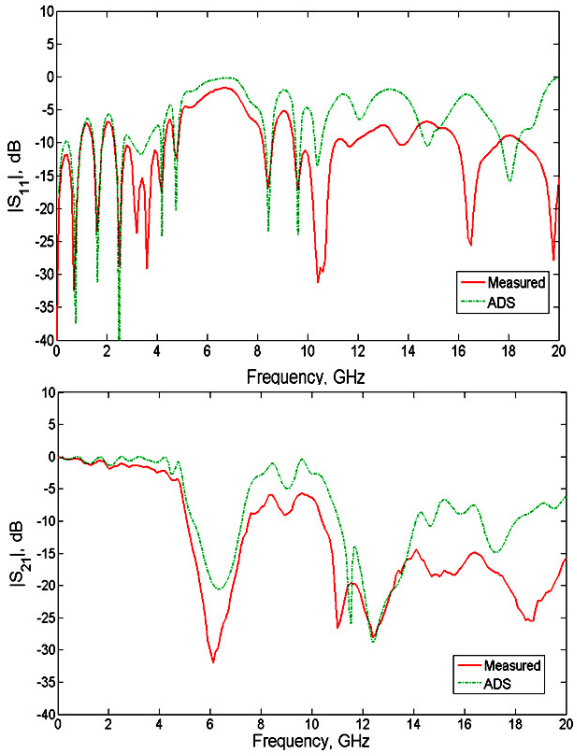

Figure 3.8: Results of the ADS Momentum simulation of the meandered line

This leads to a conclusion that some of the discrepancies can be attributed to the measurement errors. Measurement errors occur because of the microstrip-to-coaxial transitions, which are not de-embedded in the measurement, calibration errors at high frequencies. Also, the actual parameters of the manufactured test structures deviated from the values specified in the design. Another factor that limits accuracy of the measurements is the fact that some parts of the measurement setup, such as SMA cables and SMA connectors are not reliable at frequencies above 15 GHz [21].

3.3.3 Possible improvements

For accurate modeling of the circuit high frequency behavior, the frequency-dependent conductor loss must be included in the model. Generally, the contribu-

tion of the substrate loss is low compared to the conductor losses; however, at high frequencies substrate loss should be accounted for. There exist different formulations of the PML ABC, such as complex frequency shifted PML (CFS PML) and convolutional PML (CPML) [5], which yield better absorption characteristics and can be incorporated in the existing program to reduce spurious reflections errors.

On the measurement side, alternative calibration techniques such as transmission-line-thru (TRL) [21] can be employed to remove coaxial-to-microstrip discontinuities and, perhaps, provide better error correction at high frequencies. At frequencies above 15 GHz, 3.5-mm connectors and cables must be used to improve the accuracy of the measurement. Also, new substrate materials can be used to manufacture test boards with better performance at high frequencies.

CHAPTER 4

CONCLUSIONS

A numerical simulator based on the FDTD method was developed, featuring highly effective PML ABC and a plane wave voltage source based on the TF/SF formulation. The simulator was used to perform time-domain simulations of pulse propagation in various microstrip structures. Frequency-dependent scattering parameters of the line-fed rectangular patch antenna and several microstrip traces have been calculated. These results were compared with measured data and with the results of the simulation using commercial simulator. In general, a good correlation with the measured data was observed. Ways of improvement of the FDTD simulator performance along with the necessary modifications of the measurement setup were considered.

REFERENCES

[1] J. Zhao and Z. Li, "A time-domain full-wave extraction method of frequency-dependent equivalent circuit parameters of multiconductor interconnection lines," *IEEE Trans. Microwave Theory Tech.*, vol. 45, pp. 23-31, Jan. 1997.

[2] C. A. Balanis, *Advanced Engineering Electromagnetics*. New York, NY: John Wiley & Sons, 1989.

[3] Jianming Jin, *The Finite Element Method in Electromagnetics*, 2nd ed. New York, NY: John Wiley and Sons, 2002.

[4] D. de Cogan, W. J. O'Connor, and S. Pulko, *Transmission Line Matrix (TLM) in Computational Mechanics,* Boca Raton: CRC Press, 2006

[5] A. Taflove and S. C. Hagness, *The Finite-Difference Time-Domain Method* 3rd ed. Norwood, MA: Artech House, 2005.

[6] D. M. Sheen, S. M. Ali, M. D. Abonzahra, and J. A. Kong, "Application of the three-dimensional finite-difference time-domain method to the analysis of planar microstrip circuits," *IEEE Trans. Antennas Propagat.*, vol. 38, pp. 849-857, July, 1990.

[7] K. S. Yee, "Numerical solution of initial boundary value problems involving Maxwell's equations in isotropic media," *IEEE Trans. Antennas and Propagat.*, vol. 17, 1996, pp. 585-589.

[8] J. Schneider, "Numerical solutions to EM Problems I," class notes for EE 535, School of Electrical Engineering and Computer Science, Washington State University, Fall 2005.

[9] D. Sullivan, *Electromagnetic Simulation Using the FDTD Method.* Piscataway, NJ: IEEE Press, 2000.

[10] J. B. Schneider and C. L. Wagner, "FDTD dispersion revisited: Faster-than-light propagation," *IEEE Microwave and Guided Wave Lett.*, vol. 9, 1999, pp. 54-56.

[11] K. S. Kunz and R. J. Luebbers, *The Finite Difference Time Domain Method for Electromagnetics*, Boca Raton: CRC Press, 1993

[12] A. Taflove, Ed., *Advances in Computational Electrodynamics: the Finite-Difference Time-Domain Method*. Norwood, MA: Artech House, 1998.

[13] K. R. Umashankar and A. Taflove, "A novel method to analyze electromagnetic scattering of complex objects," *IEEE Trans. Electromagn. Compat.*, vol. 24, 1982, pp. 397-405.

[14] G. Mur, "Absorbing boundary conditions for the finite-difference approximation of the time-domain electromagnetic field equations," *IEEE Trans. Electromagn. Compat.*, vol. 23, 1981, pp. 377-382.

[15] R. L. Higdon, "Numerical absorbing boundary conditions for the wave equation," *Mathematics of Computation*, vol. 49, 1987, pp. 65-90.

[16] J. P. Berenger, "A perfectly matched layer for the absorption of electromagnetic waves," *J. Computational Physics*, vol. 114, 1994, pp. 185-200.

[17] Z. S. Saks, D. M. Kingsland, R. Lee, and J. F. Lee, "A perfectly matched anisotropic absorber for use as an absorbing boundary condition," *IEEE Trans. Antennas Propagat.*, vol. 43, 1995, pp. 1460-1463.

[18] S. D. Gedney, "An anisotropic perfectly matched layer-absorbing medium for the truncation of FDTD lattices," *IEEE Trans. Antennas Propagat.*, vol. 44, 1996, pp. 1630-1639.

[19] S. D. Gedney, "An anisotropic PML absorbing media for FDTD simulation of fields in lossy dispersive medium," *Electromagnetics*, vol. 16, 1996, pp. 435-449.

[20] D. M. Sullivan, "A simplified PML for use with the FDTD method," *IEEE Microwave Guided Wave Lett.*, vol. 7, 1997, pp. 184-186.

[21] T. H. Lee, *Planar Microwave Engineering: A Practical Guide to Theory, Measurement, and Circuits*. Cambridge, UK: Cambridge University Press, 2004.